Chapter 12

# Monitoring the Effects of Thermal Treatment on Properties and Performance During Battery Material Synthesis

Wesley M. Dose and Scott W. Donne

Additional information is available at the end of the chapter

http://dx.doi.org/10.5772/50882

## 1. Introduction

### 1.1. Energy supply

Utilizing an inexpensive, clean and sustainable supply of energy is one of the world's foremost challenges heading into the future. The present energy supply scenario is dominated by fossil fuels, which are both a finite resource and a substantial contributor greenhouse gas emissions. Many renewable sources of energy (e.g., nuclear, solar, wind, etc.) exist for consumer use, although they all have associated pros and cons which means they cannot be used ubiquitously across the planet [1]. As a result, the future supply of energy is not likely to be centralized in a limited number of large power stations, but rather much more distributed as smaller scale renewable energy sources are utilized.

Much has been made in the literature concerning solar energy harvesting, both in terms of photovoltaics and solar thermal. Of all the renewable forms of energy, solar energy has the capacity to completely replace society's dependence on fossil fuels. However, of course, the challenge remains to make this a reality, particularly so with the high cost of photovoltaics [1]. Another perceived problem with the use of photovoltaics, and indeed with many other renewable energy sources, is their intermittency. Whether this be over short time frames, such as with cloud cover, or extended periods of time, such as overnight, steps need to be taken to ensure the consistency of power supply. In other words, some form of energy storage must be present to complement the primary source of energy.

### 1.2. Energy storage

Energy can be stored in many different ways, some examples of which include [2]:

i. Thermal energy storage as heat;
ii. Chemical energy storage in the form of a fuel;
iii. Electrical energy storage in the form of charge separation; and
iv. Mechanical storage in the form of kinetic energy.

Each of these types of energy storage has its own set of performance characteristics in terms of the energy and power that they can deliver, ultimately meaning that they will be best suited in specific applications. Of course cyclability is also a key performance characteristic.

Chemical energy, stored as a fuel, can deliver very high specific power and energy, with reasonable efficiency, particularly when it is used in an internal combustion engine [3]. However, such a combustion reaction does little to abate the demand for fossil fuels (which are used most commonly in this domain) or the contributions to greenhouse gas emissions.

Chemical energy storage has an added advantage in the sense that it can also be released electrochemically (rather than thermally), through devices such as batteries, supercapacitors and fuel cells [4]. While the specific energy and power performance of these devices is much less than that of the internal combustion engine, their efficiency is much higher, in some instances approaching 100%, meaning that they ultimately utilize any fuel much better.

## 1.3. Batteries and battery materials

There are many battery systems available for consumer use, and over the years since commercial introduction, their performance has improved due to a combination of advances in material design and cell engineering [5]. The various battery chemistries that are available can be categorized as either primary (single use) or secondary (rechargeable) systems. The battery system that is currently receiving the most attention in the literature is based on the Li-ion chemistry. Here $Li^+$ ions are reversibly shuttled between the positive and negative electrodes in the cell, which with the use of an appropriate non-aqueous electrolyte, can achieve a potential of over 4 V [5,6]. Some of the commonly found materials in Li-ion batteries include:

i. Negative electrode materials: Li metal, carbon, $Li_4Ti_5O_{12}$, Sn and its alloys, Si and its alloys;
ii. Electrolytes: organic carbonate mixtures; e.g., 1:1 ethylene carbonate:dimethyl carbonate, ionic liquids; and
iii. Positive electrode materials: $LiMO_2$ (where M is a combination of Ni, Mn and/or Co), $LiMn_2O_4$ (and doped varieties thereof), $LiFePO_4$, $MnO_2$.

Whatever the combination of positive and negative electrode that is used, the performance of the resultant cell is quite significantly determined by the properties of the electroactive materials used, which in turn are determined by the way in which they were prepared.

Material properties such as phase purity, crystallinity and particle size (or extent of agglomeration) all affect performance.

### 1.4. Common synthetic routes

Many different synthetic routes have been used to prepare the materials mentioned in the previous section, so much so that to list them here would be excessive (note the recent review in reference [6]). Nevertheless, the more common approaches can be categorized as being based on either (i) thermal methods, (ii) solvothermal methods, (iii) mechanical methods, and (iv) electrochemical methods. It is also reasonably common to find that a combination of these methods has been used to produce the resultant material. As an example, $LiFePO_4$ can be made by first using a solvothermal process to intimately mix the precursors, with the resultant mixture then subjected to a thermal treatment to make the final product [7]. Overall, the majority of the positive electroactive materials listed above involve a thermal processing step as the last step in their synthesis.

### 1.5. Pitfalls of thermal processing methods

The overall objective of any synthesis method is to obtain the final product in the desired form for immediate use. This is particularly true for thermal synthesis methods where there is a delicate balance between heat treatment temperature and duration so as to produce the desired material. Of course the choice of these thermal parameters is also dependent on the effectiveness of precursor mixing, with various solvothermal methods being used to ensure appropriate mixing on the molecular level. Contrast this with some of the initial solid state mixing methods (grinding) used in some synthetic efforts, and the implications it has on the thermal conditions necessary [8].

Let us begin by assuming that we have sufficient mixing of our precursors, since the focus of the discussion here is on the actual thermal conditions to be used. Under these circumstances if we were to thermally treat this mixture the temperature and duration of heat treatment would determine the phase purity and crystallinity of the resultant material. Of course a higher heat treatment temperature, and a longer heat treatment duration would ensure phase purity, as well as lead to a more crystalline material. The question at this time then becomes: What is the preferred material crystallinity?

Many positive electroactive materials in Li-ion batteries require very small crystallite sizes so as to minimize $Li^+$ ion diffusion paths, which is commonly regarded as a key limiting factor in performance [7]. Therefore, excessive heat treatment temperatures and durations, while they may ensure phase purity, also lead to excessive crystallization, which is detrimental. Additionally from a commercial perspective, excessive material heating leads to a waste of energy, which can be costly. What is required, therefore, is a method for predicting the optimum heat treatment temperature and duration so as to ensure phase purity and small crystallite size.

### 1.6. This work

What we will describe here in this chapter is a method for identifying the optimum thermal synthesis conditions, and then explore their effects on the resultant material properties. The system we will use to demonstrate the approach is the heat treatment process used to remove water from the structure of γ-$MnO_2$ prior to its use in non-aqueous Li-$MnO_2$ cells. While this will be used as a representative example, the general method is applicable to any other thermally based synthetic method.

## 2. Methods

### 2.1. Preparation of starting material

The sample of γ-$MnO_2$ used in this work was prepared by anodic electrodeposition, and hence given the designation electrolytic manganese dioxide, or EMD. The cell used for electrolysis was based on a temperature controlled 2 L glass beaker in which two 144 $cm^2$ (72 $cm^2$ on either side) titanium sheets were used as the anode substrate, and three similarly sized copper sheets were used as the cathode substrate. The electrodes were arranged alternately so that each anode was surrounded on both sides by a cathode. The electrolyte was an aqueous mixture of 1.0 M $MnSO_4$ and 0.25 M $H_2SO_4$ maintained at 97°C. Electrodeposition of the manganese dioxide was conducted with an anodic current density of 65 A/$m^2$ according to the reactions:

$$\text{Anode}\,(\text{Ti}):\quad Mn^{2+} + 2H_2O \longrightarrow MnO_2 + 4H^+ + 2e^- \tag{1}$$

$$\text{Cathode}\,(\text{Cu}):\quad 2H^+ + 2e^- \longrightarrow H_2 \tag{2}$$

$$\text{Overall}: Mn^{2+} + 2H_2O \longrightarrow MnO_2 + 2H^+ + H_2 \tag{3}$$

The overall process was carried out for three days, during which time the electrolyte $Mn^{2+}$ concentration was of course depleted, while the $H^+$ concentration increased. To counteract this, and hence maintain a constant electrolyte concentration over the duration of the deposition, a concentrated (1.5 M) $MnSO_4$ solution was added continually at a suitable rate to replenish $Mn^{2+}$ and dilute any excess $H_2SO_4$ produced. Under these conditions control of the solution conditions was typically maintained to within ±2%.

After deposition was complete, the solid EMD deposit was mechanically removed from the anode and broken into chunks ~0.5 cm in diameter, and then immersed in 500 mL DI water to assist in the removal of entrained plating electrolyte. The pH of this chunk suspension was adjusted to pH 7 with the addition of 0.1 M NaOH. After ~24 h at a pH of 7 the suspension was filtered and the chunks then dried at 110°C. After drying the chunks were then milled to a -105 μm powder (mean particle size ~45 μm) using an orbital zirconia mill.

The powder was then suspended in ~500 mL of DI water and its pH again adjusted to 7 with the further addition of 0.1 M NaOH. When the pH had stabilized, the suspension was filtered and the collected solids dried at 110°C. When dry the powdered EMD was removed from the oven, allowed to cool to ambient temperature in a dessicator and then transferred to an airtight container for storage.

## 2.2. Thermogravimetric (TG) analysis

TG analysis was conducted using a Perkin Elmer Diamond TG/DTG controlled by Pyris software. Approximately 10 mg of γ-$MnO_2$ sample was added to an aluminium sample pan and placed into the analyser. The same mass of α-$Al_2O_3$ in a similar aluminium pan was used as the reference material for DTA measurements. With the sample and reference materials loaded, and the furnace closed, dry nitrogen gas was passed over the sample at 20 mL/min for 30 minutes prior and during the heating profile. The heating profile applied to the sample was essentially a linear ramp at rates ranging from 0.25°-10°C/min.

## 2.3. Material characterization

The structure of the materials generated in this work were identified by X-ray diffraction using a Phillips 1710 diffractometer equipped with a Cu K$\alpha$ radiation source ($\lambda$=1.5418 Å) and operated at 40 kV and 30 mA. The scan range was from 10° to 80° 2θ, with a step size of 0.05° and a count time of 2.5 s. Analysis of the diffraction patterns was carried out by fitting a Lorentzian lineshape to individual peaks, with the fitting parameters then used to calculate structural properties such as the fraction of pyrolusite ($P_r$; as described by Chabre and Pannetier [9]) and the unit cell parameters.

Morphology was examined by gas adsorption using a Micromeritics ASAP 2020 Surface Area and Porosity Analyser. A representative 0.10 g sample of the manganese dioxide material was degassed under vacuum at 110°C for 2 h prior to analysis. An adsorption isotherm was then determined over the partial pressure ($P/P_0$) range of $10^{-7}$-1 using $N_2$ gas as the adsorbate at 77 K. The specific surface area was extracted from the gas adsorption data using the linearized BET isotherm [10] in the range $0.05<P/P_0<0.30$, while the pore size distribution was determined using a Density Functional Theory-based approach (Micromeritics DFTPlus V2.00).

The composition of the materials was determined using two consecutive potentiometic titrations (Pt indicator and SCE reference electrode) as outlined in Vogel [11]. A blank titration was carried out first in which 10 mL of acidified 0.25 M ferrous ammonium sulfate ($NH_4FeSO_4.6H_2O$, BDH Chemicals, 99%) was titrated with a standardised 0.03 M potassium permanganate solution ($KMnO_4$, Ajax Finechem, 99%; standardized using the oxalate method [11]), and the volume of permanganate added to reach the end point denoted as $V_0$. Sample analysis was conducted by digesting 0.050 g of the manganese dioxide being studied into another 10 mL aliquot of the acidified 0.25 M ferrous ammonium sulfate solution. After complete dissolution the resultant solution was then titrated using the same 0.03 M permanganate solution, with the volume to reach the end point recorded as $V_1$. For this

titration it is important to stop at or just after the end point has been attained. To the solution resulting from the first titration ~6 g of tetra-sodium pyrophosphate ($Na_4P_2O_7.10H_2O$, Ajax Finechem, 99%) was added and allowed to dissolve. The pH of this solution was then adjusted to lie within the range 6-7 by the drop-wise addition of ~0.20 M sulfuric acid. The second potentiometic titration was performed using the same 0.03 M permanganate solution, and the volume to reach the end point recorded as $V_2$. The value for x in $MnO_x$ was then calculated using:

$$x=1+\frac{5(V_0-V_1)}{2(4V_2-V_1)} \tag{4}$$

The total manganese content in the sample can be found from the second titration by taking into account the amount of manganese added through the addition of permanganate in the first titration. Using this result, and the dry mass of the manganese dioxide sample, found by subtracting the mass of surface water lost from the sample after heating at 110°C (%$H_2O$(<110°C)) from the original mass, the total manganese content (%Mn) can be found using:

$$\%Mn=\frac{n_{Mn}}{n_{MnO_2(dry)}}\times 100 \tag{5}$$

To calculate the relative proportion of manganese (III) and (IV) species (%Mn(III) and %Mn(IV) respectively), we have:

$$\%Mn(III)=(4-2x)\times\%Mn \tag{6}$$

$$\%Mn(IV)=(2x-3)\times\%Mn \tag{7}$$

Finally, the cation vacancy fraction (CVF) can be found by taking into account the percentage structural water (i.e., water removed after heating at 400°C, but above 110°C, (%$H_2O$(>110°C)), found by considering the difference in mass after heating the sample at 400°C for 2 h, and using:

$$CVF=\frac{m}{m+2} \tag{8}$$

where

$$m=(2-x)+\frac{M_{Mn}\times\%H_2O(>110°C)}{M_{H_2O}\times\%Mn} \tag{9}$$

and $M_{Mn}$ and $M_{H_2O}$ are the molar masses of manganese and water, respectively.

## 2.4. Thermal treatment of EMD

Approximately 10 g of EMD was heated in an alumina boat crucible by a Eurotherm HTC1400 furnace with a static air atmosphere set at the required temperature. After the elapsed isothermal heating time, the sample was removed from the oven and allowed to cool to room temperature.

### 2.5. Electrochemical performance

To evaluate the electrochemical performance the heat treated materials prepared were first thoroughly mixed with graphite and polyvinylidene fluoride, in a 1:8:1 ratio. Around 0.30 g of this mixture was compressed in a 10 mm die press under 1 t into a disk electrode ~1 mm thick. The electrodes were dried at 110°C under vacuum and accurately weighed prior to introduction into an Ar-filled dry box, where cell construction took place.

CR2032 size coin cells were constructed for electrochemical testing. The coin cells were comprised of a heat treated EMD (HEMD) cathode, lithium metal anode, with electrolyte made up from 1 M $LiPF_6$ (Sigma-Aldrich (≥99.99%) in 1:1 w/w of ethylene carbonate (EC, Sigma-Aldrich 99%) and dimethyl carbonate (DMC, Sigma-Aldrich 99+%). A Celgard 2400 micro-porous separator was used in these cells. After construction, cells were left to equilibrate for 3-4 days before being used for electrochemical testing.

The electrochemical characteristics of the cells prepared were assessed using a Perkin-Elmer VMP multichannel potentiostat/galvanostat on which a modular galvanostatic discharge program was performed at rates of 2, 5, 10 and 20 mA/g of active material.

## 3. Data analysis

### 3.1. Starting material properties

The compositional, morphological and structural data for the starting EMD sample are shown in the first row of Table 1. While the details of these initial properties and the resulting changes to the measured parameters as a result of heat treatment will be discussed in detail later, we note here that the EMD chosen for this work is a typical EMD sample. The composition of samples prepared via electrolysis can vary considerably depending on the experimental deposition conditions. We find that the compositional data collected for our starting EMD fit comfortably within the typical range for samples termed EMD [12]. The structure of the starting EMD, as measured by XRD, is shown in Figure 1. The Miller indicies for the peaks in the starting EMD pattern are labelled assuming an orthorhombic unit cell.

| | Composition | | | | | |
|---|---|---|---|---|---|---|
| **Temp (°C)** | **Mn(T) (%)** | **Mn(IV) (%)** | **Mn(III) (%)** | **CVF** | **%$H_2O$ (>110°C)** | **%$H_2O$ (<110°C)** |
| 25 | 59.45 | 55.34 | 4.11 | 0.081 | 2.13 | 4.11 |
| 200 | 59.00 | 55.03 | 3.98 | 0.051 | 1.67 | 2.73 |
| 250 | 61.47 | 57.28 | 4.20 | 0.027 | 1.60 | 1.81 |
| 300 | 61.82 | 55.22 | 6.60 | 0.008 | 1.66 | 1.41 |
| 350 | 60.94 | 54.94 | 6.00 | 0.000 | 0.94 | 0.84 |
| 400 | 60.41 | 53.79 | 6.61 | 0.000 | 1.15 | 0.90 |

| | Morphology | | | | Structure | | | | |
|---|---|---|---|---|---|---|---|---|---|
| Temp (°C) | BET SA ($m^2/g$) | Micro-pore Volume ($cm^3/g$) | Meso-pore Volume ($cm^3/g$) | Temp (°C) | $P_r$ | $a_0$ (Å) | $b_0$ (Å) | $c_0$ (Å) |
| 25 | 37.22 | 0.0074 | 0.0293 | 25 | 0.34 | 4.47 | 9.55 | 2.83 |
| 200 | 36.68 | 0.0071 | 0.0358 | 200 | 0.50 | 4.41 | 9.35 | 2.85 |
| 250 | 32.46 | 0.0047 | 0.0327 | 250 | 0.52 | 4.43 | 9.33 | 2.85 |
| 300 | 30.67 | 0.0038 | 0.0348 | 300 | 0.73 | 4.42 | 9.22 | 2.86 |
| 350 | 24.90 | 0.0021 | 0.0401 | 350 | 0.83 | 4.42 | 9.11 | 2.87 |
| 400 | 27.49 | 0.0034 | 0.0392 | 400 | 0.84 | 4.42 | 9.20 | 2.87 |

**Table 1.** Composition, morphology and structure of the starting and heat treated EMD samples

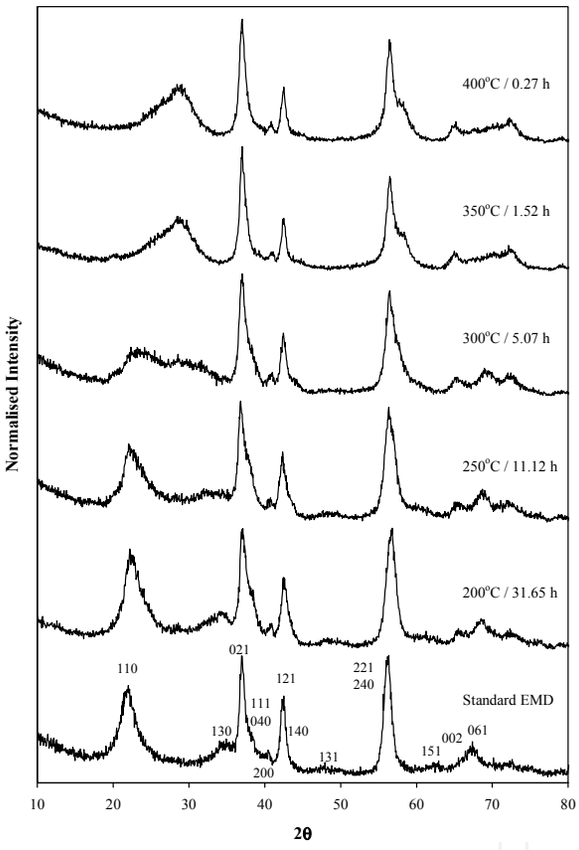


**Figure 1.** XRD pattern of the starting EMD showing the γ-$MnO_2$ structure, with the corresponding Miller indices indexed using an orthorhombic unit cell, and XRD patterns for the heat treated EMD.

## 3.2. Thermogravimetric analysis

The thermogravimetric (TG) and differential thermogravimetric (DTG) data for the thermal decomposition of the EMD sample at the various heating rates are shown in Figures 2 and 3, respectively. The initial loss in mass up to ~120°C is due to the removal of physisorbed water from the EMD surface. Manganese oxides are well known for their ability to adsorb water [13],

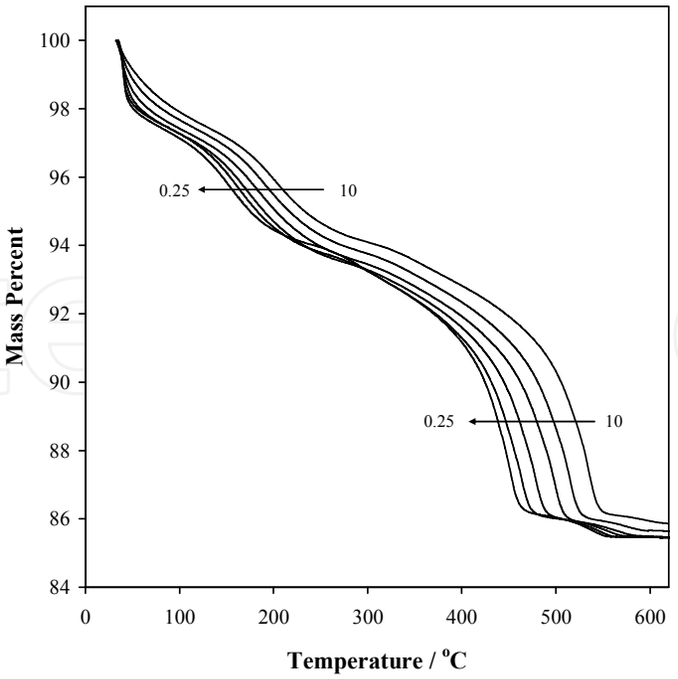


**Figure 2.** TGA data for the EMD sample used in this work recorded at rates of 0.25, 0.5, 1.0, 2.5, 5.0 and 10.0°C/min.

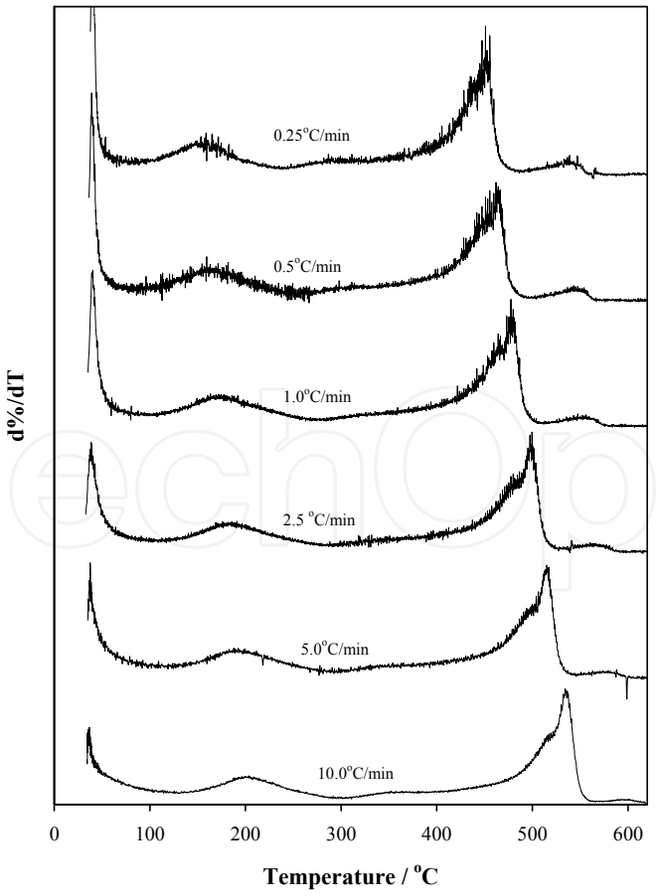


**Figure 3.** Differential thermogram (DTG) for the EMD sample heated at different heating rates.

so it is not surprising that 2-3% of the initial sample mass is physisorbed water. The broad peak at ~200°C in the DTG relates to the removal of structural water; i.e., protons associated with cation vacancies and Mn(III) ions within the manganese dioxide structure. The sharper peak at ~500°C relates to the thermal reduction of the $MnO_2$ to form $Mn_2O_3$. The use of faster heating rates has shifted the decomposition temperature to higher values, possibly as a result of slow reaction kinetics and/or since less time is allowed for the equivalent reaction. It is also possible that the thermal conductivity of the EMD contributed to this effect, although with the use of a relatively small sample size (~10 mg) its contribution is expected to be minor.

### 3.3. Multiple curve isoconversional analysis

In this analysis, we will be considering the first step in the EMD thermal decomposition; i.e., the process of removing water from the structure beginning at ~175°C, since this is most important when the material is to be used in a non-aqueous battery system.

The first step in the analysis was background correction of the DTG data. To do this an exponential background curve was fitted to the data surrounding the peak for each heating rate used. The resulting curve after background correction describes the processes occurring in this region, as shown in Figure 4 for a heating rate of 10°C/min. The normalized extent of conversion ($\alpha$) was then found by numerical integration of the background-corrected DTG data, with the normalization being carried out by expressing each point relative to the maximum area determined. A plot of $\alpha$ as a function of temperature for the range of heating rates considered is shown in Figure 5. From this data the temperatures corresponding to a pre-defined set of $\alpha$ values can be found for each heating rate, as shown in Figure 6.

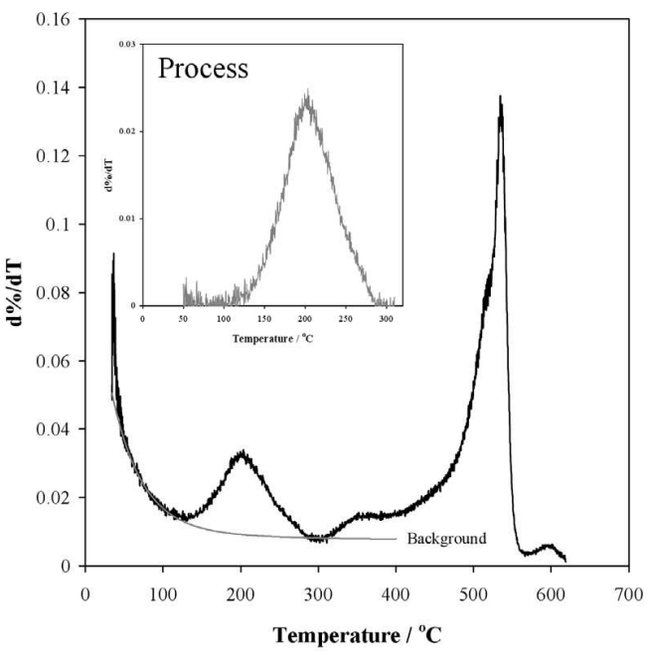


**Figure 4.** Fitting of DTG data for heating rate 10°C/min with background curve and resulting process.

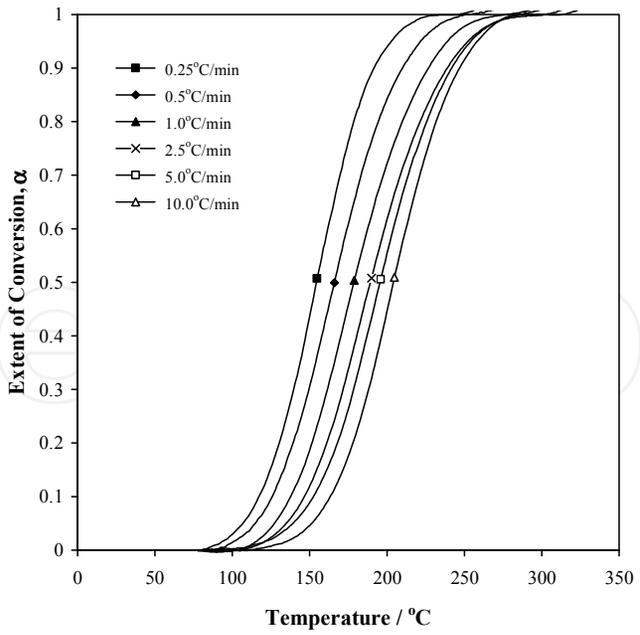


**Figure 5.** Extent of conversion versus temperature for the different heating rates.

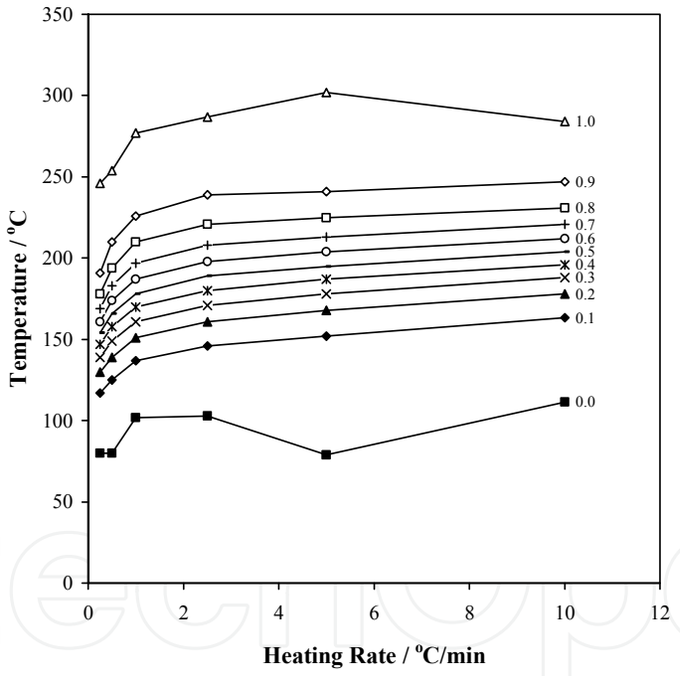


**Figure 6.** Variation of temperature with heating rate for given extent of conversion.

Kinetic analysis using this method is conventionally applied to the data corresponding to $\alpha$=0 for the different heating rates. However, since we have access here to the temperature corresponding to various extents of conversion for different heating rates, and the fact that we will apply the method used for $\alpha$=0 to all $\alpha$ values, then it will be interesting to observe how the resultant kinetic parameters change. Kinetic analysis is based on the rate equation:

$$\beta \frac{d\alpha}{dT} = Af(\alpha)\exp\left(-\frac{E_A}{RT}\right) \quad (10)$$

where $A$ is the pre-exponential factor ($min^{-1}$), $\beta$ is the heating rate (°C/min), $E_A$ is the activation energy (J/mol), the term $f(\alpha)$ represents the model chosen to represent the mechanism of thermal decomposition, and all other symbols have their usual significance. In this case we will use $f(\alpha)=1-\alpha$ as our decomposition model [14]. Separation of variables leads to:

$$\frac{d\alpha}{f(\alpha)}=\frac{A}{\beta}\exp\left(-\frac{E_A}{RT}\right)dT \tag{11}$$

and then integration of the left-hand side from 0 to $\alpha_i$ in Eqn. 11, gives:

$$F(\alpha_i)-F(0)=\int_0^{T_i}\frac{A}{\beta}\exp\left(-\frac{E_A}{RT}\right)dT \tag{12}$$

where $F$ represents the integrated form of $f(\alpha)$, and $T_i$ corresponds to the temperature at $\alpha_i$. Upon rearrangement we can write:

$$\beta=\int_0^{T_i}\frac{A}{F(\alpha_i)-F(0)}\exp\left(-\frac{E_A}{RT}\right)\,dT \tag{13}$$

This integration was performed numerically using the trapezium method and optimised to fit the experimental data using a linear least squares regression. Consequently, the dependence of activation energy on the extent of conversion and the pre-exponential factor was found, as shown in Figure 7. With the exception of the first point at $\alpha$=0 (which was likely due to the noisy data for these conditions, cf. Figure 6), the activation energy clearly increases with extent of conversion, ranging from 109-250 kJ/mol.

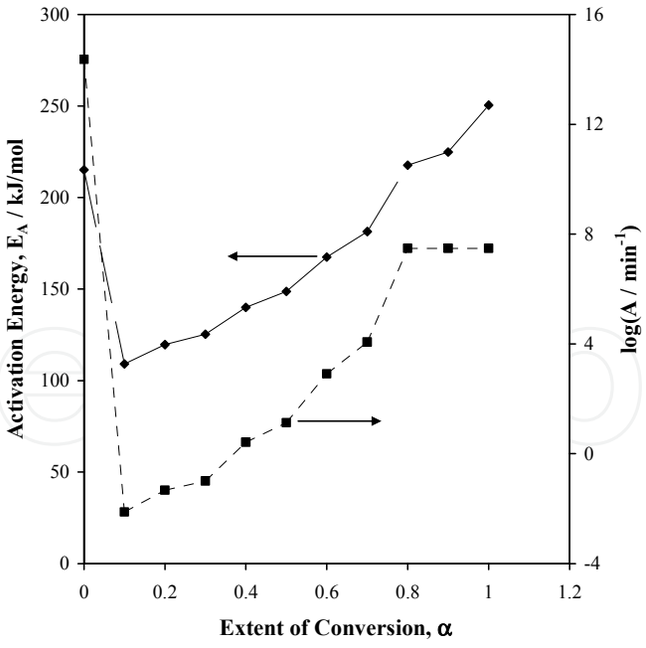


**Figure 7.** Activation energy and pre-exponential factor for process occurring against extent of conversion calculated using the first order kinetic analysis.

Before going further, an additional comment needs to be made regarding the choice of thermal decomposition model ($f(\alpha)$) used in the analysis. Each of the models listed in

reference [14] were examined here using this approach. Firstly, despite the broad range of curve shapes ($\alpha$ vs. $T$) that these models generate, no single one was able to fit satisfactorily to the experimental data – hence the use of the incremental approach in our analysis. As we will discuss later, this provides strong supporting evidence for multiple weight loss processes occurring. Additionally, with the application of the incremental approach, it was noted that for each thermal decomposition function ($f(\alpha)$) used, the measured activation energy was similar to that reported in Figure 7, with similar variation in the activation energy across the extent of conversion ($\alpha$). Again, this suggests the presence of multiple weight loss processes, as well as providing us with some confidence for using the first order $f(\alpha)=1-\alpha$ expression over the range used. Finally, the use of this model enables us to quite easily calculate the required isothermal time necessary to achieve a specified extent of conversion.

### 3.4. Single curve incremental isoconversional analysis

Another approach to solving the rate expression in Eqn. 10 is the incremental integral method [14,15]. This method can also be used to take into account the dependence of the kinetic parameters on the extent of conversion, focussing instead on an individual TG experiment rather than a range of different heating rate experiments. In this case, the Runge-Kutta method, an iterative technique for the approximation of ordinary differential equations, was used to solve Eqn. 10. This method uses the previous point ($\alpha_n$, $T_n$) to approximate the next ($\alpha_{n+1}$, $T_{n+1}$), by using the size of the interval between the points ($h$) and an estimated average of the slopes. To begin we have the initial condition:

$$\alpha(T_0)=a_0=0 \tag{14}$$

Then, using the Runge-Kutta method, $\alpha_{n+1}$ and $T_{n+1}$ are given by:

$$\alpha_{n+1}=\alpha_n+\frac{1}{6}h(k_1+2k_2+2k_3+k_4) \tag{15}$$

$$T_{n+1}=T_n+h \tag{16}$$

where $h$ is the size of the interval (1°C was used in this analysis), and:

$$k_1=f(T_n,\alpha_n) \tag{17}$$

$$k_2=f\left(T_n+\frac{h}{2},\alpha_n+\frac{hk_1}{2}\right) \tag{18}$$

$$k_3=f\left(T_n+\frac{h}{2},\alpha_n+\frac{hk_2}{2}\right) \tag{19}$$

$$k_4=f(T_n+h,\alpha_n+hk_3) \tag{20}$$

where the function $f(T,\alpha)$ is implied by Eqn. 10. This gives rise to a theoretical curve for the extent of conversion against temperature, which can be fitted to the experimental curve using linear least squares regression in a restricted range of $\alpha$ (hence employing the incremental integral method), by varying values for the activation energy, $E_A$, and the pre-

exponential factor, *A*. Figure 8 demonstrates how the activation energy changes as a function of extent of conversion and heating rate for this analysis method. Because the focus here is on just one data set, particular attention was paid to the fitting procedure to ensure that a global minimum was determined. This was achieved by repeating the fitting multiple times, from different starting points. In each case, across the complete $\alpha$ range and for each heating rate used, the same result was achieved.

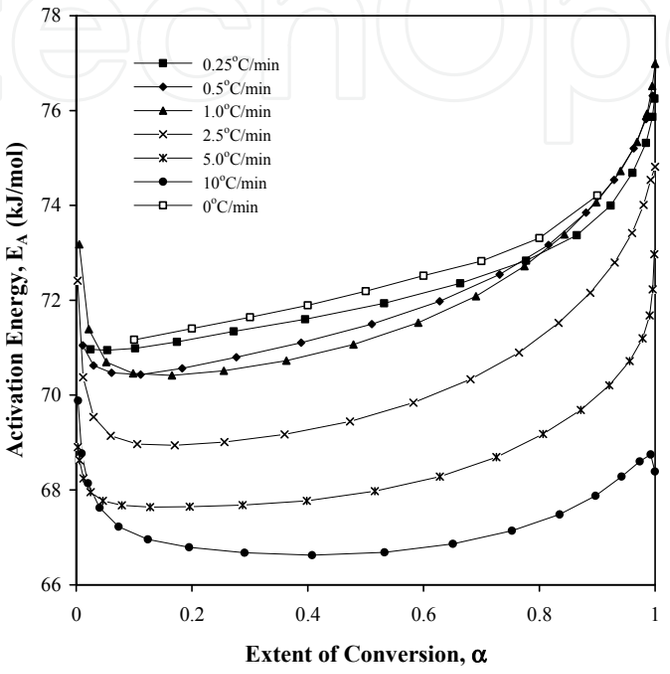


**Figure 8.** Activation energy with respect to extent of conversion for the different heating rates.

The pre-exponential factor for all analyses remained essentially constant at a value of $(5.3\pm0.8)\times10^6$ $min^{-1}$, where the error analysis here takes into account the variation in the calculated *A* value.

Overall, the calculated activation energy for the mass loss associated with the thermal decomposition of γ-$MnO_2$ fell within the rather narrow range 66-77 kJ/mol. Nevertheless, within this range there were some systematic changes observed. For all heating rates there was a minimum, or for lower heating rates, a plateau in the activation energy within the extent of conversion range $0.1<\alpha<0.7$. At both higher and lower $\alpha$ values the activation energy increased. This increase is interesting in that it tells us something about the availability of energy or heat, as well as reactants, to affect the thermal transformation. At low $\alpha$ values, corresponding to lower temperatures, there is insufficient heat to activate the reaction, so for all intents and purposes, the activation energy is much larger than normal because very little reaction is occurring. Conversely, at higher $\alpha$ values there is a relatively low concentration of unreacted species available to actually undergo the thermal transformation, and as such the rate of the thermal transformation here is also inhibited (manifested as an increase in activation energy) since reactant concentration is also a

limiting factor in chemical reactions. What is also interesting about the data in Figure 8 is the general decrease in calculated activation energy as the heating rate was increased. This is quite clearly demonstrated in Figure 9, which shows how the activation energy at $\alpha$=0.5 changes with heating rate. The data in this figure indicates that there are two heating rate regions for which there is an exponential decrease in calculated activation energy with heating rate. The cause of this may lie in the apparently less than ideal thermal transfer of heat from the furnace to the sample during the TG experiment. Whether there is a thermal gradient within the powdered sample in the TG pan, or within individual sample particles, it does mean that the thermal decomposition reaction will be occurring at different rates within the sample and/or individual particles. Certainly at higher heating rates this thermal gradient will be much more pronounced, meaning that there is expected to be a greater error in the estimated activation energy when determined at faster heating rates. While the thermal conductivity of manganese dioxide is, to the best of our knowledge, not available in the literature, other similar metal oxides have relatively high thermal conductivities, as shown in Table 2 [16]. Typical thermal conductivity values lie within the range 2-30 W $m^{-1}$ $K^{-1}$. Of these, the value for titanium dioxide (3.8 W $m^{-1}$ $K^{-1}$) is most likely very similar to manganese dioxide given the proximity of the metals to each other in the periodic table, and the iso-structural nature of the corresponding oxides. This relatively low value does imply that there will be a reasonable thermal gradient across each particle. To eliminate the effect of thermal conductivity, the exponential relationship between heating rate and calculated activation energy was extrapolated to predict the activation energy under the hypothetical condition of a 0°C/min heating rate. This extrapolated data is also shown in Figure 8, and is expected to more closely represent the true activation energy for this thermal decomposition process.

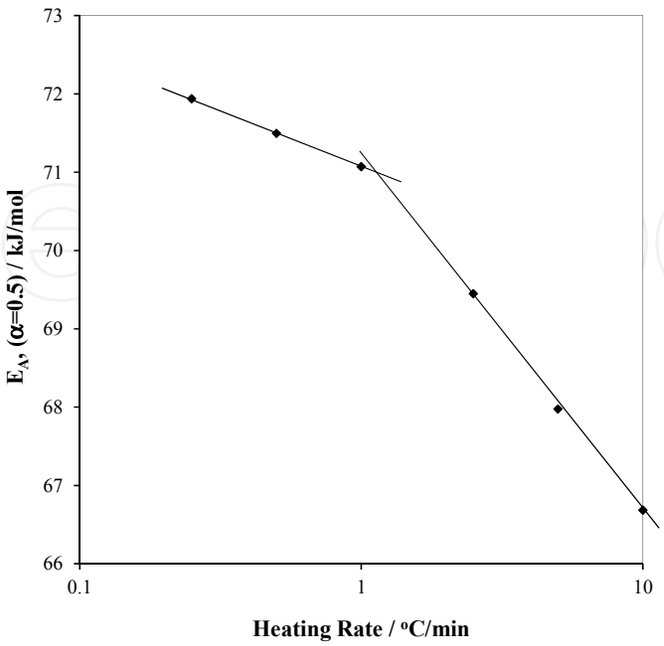


**Figure 9.** Activation energy (for $\alpha$=0.5) as a function of heating rate.

| Metal Oxide | Thermal Conductivity (W $m^{-1}$ $K^{-1}$) |
|---|---|
| $Al_2O_3$ (sintered) | 26 (373 K) |
| $BaTiO_3$ | 6.2 (300 K) |
| $Fe_3O_4$ (magnetite) | 7.0 (304 K) |
| MnO | 3.5 (573 K) |
| $SiO_2$ (fused silica) | 1.6 (373 K) |
| $SrTiO_3$ | 11.2 (300 K) |
| $TiO_2$ | 3.8 (400 K) |

**Table 2.** Thermal conductivity of selected metal oxides [16].

As was mentioned previously, the systematic variation in the activation energy, as shown in Figure 8 and highlighted specifically in Figure 9, quite nicely validates the use of this method for the thermal analysis of kinetic parameters. The International Confederation for Thermal Analysis and Calorimetry (ICTAC) has recommended that single scan methods of analysis be avoided where possible (see for example reference [17]). However, in this work the activation energies obtained were not just based on one analysis. In fact, what we have shown here is that the systematic variation within the activation energy over two orders of magnitude change in heating rate (Figure 9) not only provide us with considerable confidence in the resultant data, but also allows us to extrapolate to what the theoretical activation energy would be at a 0°C/min heating rate. This latter outcome has not been reported previously, at least for this system, and in actual fact represents a novel approach to determining an activation energy that is free of experimental artefacts, such as thermal transfer of heat to the sample.

Finally, the kinetic parameters determined for the water loss process can be used to calculate the required isothermal time to achieve complete conversion of the material ($\alpha$=1), i.e., completely remove water from the material, at a range of temperatures. This value can be found by employing the Arrhenius equation to calculate the rate constant (k) and subsequently, assuming first order kinetics, the heating time can be determined. This was performed for the heating rate 1°C/min, and is shown in Table 3.

| Temperature (°C) | Heating time (h) |
|---|---|
| 200 | 31.65 |
| 250 | 11.12 |
| 300 | 5.07 |
| 350 | 1.52 |
| 400 | 0.27 |

**Table 3.** Isothermal heating regimes to achieve complete conversion of the water loss process.

## 3.5. Comparison of methods

The first order analysis of the kinetics has shown that the activation energy for the loss of water from the manganese dioxide structure increased relatively linearly with extent of

conversion, varying from ~109 kJ/mol at $\alpha$=0.1 to ~250 kJ/mol at $\alpha$=1.0. On the other hand the incremental integral method led to an activation energy of ’66—76 kJ/mol throughout the majority of the thermal transformation, with slightly higher values at both lower and higher extents of the conversion. Clearly there are significant differences in the results obtained from the application of the two kinetic analysis methods, and these differences need to be addressed.

From a purely statistical perspective, the use of multiple experiments to produce data for analysis is bound to contain more variation than just using a single experiment. Under these circumstances, therefore, we might expect that the incremental integral approach should inherently be more reliable than the first order analysis method. Nevertheless, the contribution to the total variation in the analysis made by the individual TG experiments is expected to be quite small, certainly not enough to account for the significant difference between the two methods.

As part of the analysis, a background correction of the DTG data was employed to focus specifically on the mass loss process of interest; i.e., the loss of structural water from the manganese dioxide. While this background correction was applied to all of the data reported here, it was in no way constant between experiments. Furthermore, the shape of the background correction curve was arbitrarily chosen to be exponential. The point being made is that the background correction being made could have easily over- or under-compensated its contribution to the total response, thus inducing some variability between experiments. This would certainly suggest that the incremental integral approach should be the preferred method.

Another likely contributor to variability in the analysis is the thermal conductivity of the manganese dioxide in relation to the heating rate used. Despite the fact that only a small quantity of material (~10 mg) was used in each experiment, the rate with which heat is transferred through the sample is very critical in determining the validity of the resultant information, particularly so since the kinetic analysis model assumes that the sample temperature is uniform throughout. As has already been mentioned, the thermal conductivity of manganese dioxide is not available in the literature; however, the thermal conductivity of similar materials (e.g., titanium dioxide) does suggest that there may be thermal gradients within the manganese dioxide, particularly with the use of fast heating rates. Therefore, those experiments that make use of the higher heating rates could be judged as having a higher relative error compared to those using slower heating rates. Therefore, the incremental integral approach, particularly for those experiments employing a slower heating rate, is most likely to be the preferred method.

As a final comment, the first order kinetic analysis involved the use of separation of variables to solve Eqn. 10. An inherent assumption made with this approach is that the extent of conversion is independent of temperature, when in fact this is not the case given the thermal gradients within the manganese dioxide sample and the fact that the conversion process we are examining covers a very broad temperature range. Under these

circumstances, while the data we have collected shows a nice asymptotic change with heating rate (Figure 9), the assumptions made in the numerical analysis do not lead to an accurate estimate of the activation energy, again implying that the incremental integral approach is superior.

# 4. Material effects

## 4.1. Introduction

In the preceding discussion we found the incremental iso-conversional approach for analysing thermogravimetric data to be the favourable method to investigate the kinetics of water loss during the heat treatment of a γ-$MnO_2$ sample. Using the kinetic parameters from this analysis, particular heating regimes at a selection of temperatures were devised to prepare materials with a theoretical complete water loss ($\alpha$=1), thereby avoiding the use of excessive temperatures and/or times. We now consider the effects of these optimised thermal treatment regimes on the heat treated material structure, composition and morphology. The electrochemical characteristics of these heat treated EMD samples are examined and the observed changes in the material properties used to relate the electrochemical performance to the material properties.

## 4.2. Heat treated material properties

The XRD patterns for the heat treated $MnO_2$ samples are shown in Figure 1. The most obvious changes in these XRD patterns as a result of heat treatment are (i) the merging of the (110) (~22° 2θ) and the (130) (~36° 2θ) lines in the starting γ-$MnO_2$ to form a single peak at ~29° 2θ in the sample heat treated at 400°C; (ii) clearer separation of the (221) and (240) peaks at ~56° 2θ by 400°C; and (iii) disappearance of the peak at ~68° 2θ and the emergence of two peaks at ~66° 2θ and ~73° 2θ. The extent of conversion from the γ-$MnO_2$ phase, which predominantly displays a ramsdellite composition, to the more thermodynamically stable pyrolusite structure can be determined quantitatively by calculation of the fraction of pyrolusite ($P_r$) in the samples using the method outlined by Chabre and Pannetier [9]. These results are listed in Table 1. Interestingly, these changes are consistent with literature investigating γ-$MnO_2$ heat treated at various temperatures for 24 hours [18,19], indicating a progressive structural conversion with increasing heat treatment temperature. This is despite the largely different experimental heating times used. The similarities indicate that this conversion is mostly influenced by the thermodynamics of the heating process rather than the kinetics. For instance, samples heated at lower temperatures (i.e., 200°C and 250°C) have begun the conversion from γ→β-$MnO_2$, although this process is clearly retarded by insufficient thermal energy to drive this process to completion. This is further supported by comparing the data recorded at 400°C using this analysis method (16 mins heating time) with a sample heated at the same temperature for 7 days. In both cases, a $P_r$ value of 0.84 was calculated from the XRD data suggesting few or no kinetic limitations for this process at the elevated temperature.

The structural changes can be further elucidated by consideration of the unit cell parameters (determined from the XRD patterns of these materials assuming an orthorhombic unit cell) as a function of heat treatment temperature. The unit cell parameters for the starting EMD were $a_0$ = 4.468 Å, $b_0$ = 9.554 Å and $c_0$ = 2.833 Å, which is an expansion in the *a-b* plane, but a slight contraction in the *c* direction, compared with ramsdellite [20]. The unit cell parameters for the heat treated materials are shown in Table 1. The decrease shown for both the $a_0$ and $b_0$ parameters represents a structural contraction in these directions, while the steady increase in the $c_0$ parameter indicates lattice expansion in this direction. By considering the differences in the crystal structures of $\gamma$-$MnO_2$ and pyrolusite, it is clear that the main differences are found in the *a-b* plane. Since the unit cell is found to contract along both these directions, this suggests that ion (Mn(IV)) movement predominates in these directions during heat treatment. The excess of edge sharing octahedra in a uniform array in the *c* direction, without any vacancies present to compensate or provide a buffer for the close proximity of the Mn(IV) ions, results in expansion in this direction [18].

The changes in BET surface area for the HEMD samples are shown in Table 1. The relatively high surface area for these materials indicates that they are quite porous. Most evident from this data is the general decrease in surface area as temperature increases, barring a slight increase between the 350°C and 400°C samples. Given the structural changes occurring during heat treatment, the decreasing surface area suggests that the pores in EMD are removed as Mn(IV) ions diffuse through the structure, creating a more defect free and crystalline material [18]. The slight increase in surface area for the 400°C material is likely to be caused by slow kinetics for this process (relating to the much shorter heating period applied to this material), thus not allowing for the completion of pore collapse. Noticeably, at the lower temperatures (e.g., 200°C), the surface area has not decreased significantly from the original value. This is likely to be connected to insufficient activation energy at the relatively low temperature to drive Mn(IV) diffusion, a factor responsible for pore closure. Table 1 also lists the changes in micro- (<2 nm) and meso-pore (2-50 nm) structures as a result of heat treatment. Clearly, heat treatment causes the collapse of micro-pores, while an increase in the meso-pore volume was observed. The increase in the micro-pore volume for the 400°C material with respect to the 350°C sample indicates that kinetic limitations in the collapse of these pores is responsible for the increase in BET surface area for this material.

A comparison of how the structural changes relate to morphological changes clearly portrays the key differences in the HEMD materials prepared. Figure 10 compares the changes in the orthorhombic unit cell volume with BET surface area. From this data, it is evident that between the temperatures tested, small changes in BET surface area can relate to large structural changes (e.g., between the standard EMD and 200°C material), or vice versa. Generally, however, the interplay of the thermodynamics and kinetics influencing the variation in these parameters leads to an approximately exponential decrease in unit cell volume with respect to BET surface area. Decreases in the unit cell volume can be attributed to manganese ions within the structure having sufficient thermal energy to move to positions consistent with pyrolusite, thus causing intra-crystallite rearrangement within the material. Conversely, changes in BET surface area relate to either the sintering of crystallites

(both intra- and inter-) by joining together across the pores thus resulting in pore closure, or the opening of existing pores.

The underlying assumption in the preparation of these samples is that structural water, which is associated with defects (i.e., Mn(III) and cation vacancies), has been completely removed from the material. There is an expectation then that each of the HEMD samples will have no Mn(III), cation vacancies or water removed above 110°C (%$H_2O$(>110°C)). However, the compositional data for the HEMD samples (Table 1) shows that this is not the case. In light of this, the trends evident in these parameters provide important insights into the kinetic and thermodynamic limitations of the heat treatment under the set conditions and at these temperatures. The data for these samples show that the total manganese content (%Mn(T)) increases with heating temperature to an optimum at 300°C. This increase relates to the rearrangement of Mn(IV) ions to form a more defect free structure as cation vacancies are annealed via loss of structural protons. As a consequence, a steady decrease in the cation vacancy fraction is observed with heating temperature. The gradual decline in this parameter suggests that as the thermal energy required for this process is met by the higher temperatures, vacancy removal is able to proceed to a greater degree. After heat treatment at 350°C and 400°C, vacancy defects and associated water have been completely removed from the structure, indicating that these heating regimes have provided sufficient thermal energy to complete this process, without any kinetic limitations.

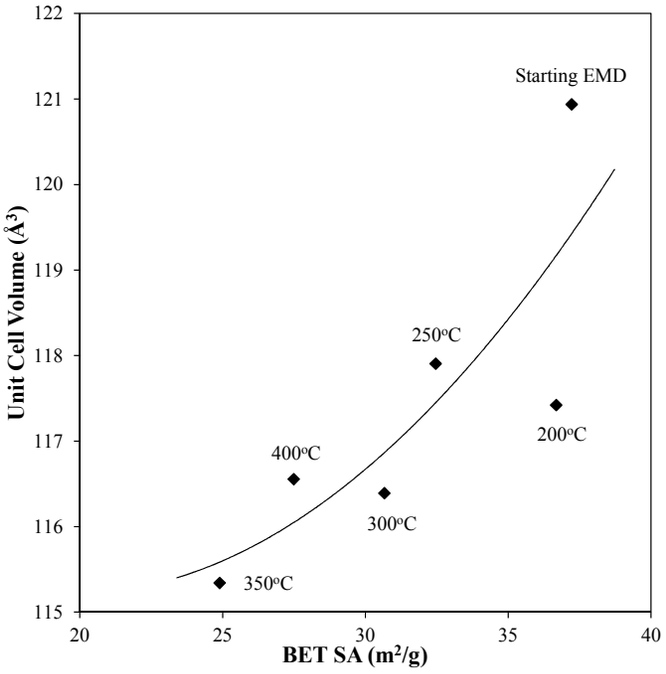


**Figure 10.** Relationship between BET surface area and unit cell volume for heat treated EMD samples.

The trends in Mn(III) and Mn(IV) percentages are confused to some degree due to a number of processes taking place during the heating experiment. First, the oxidation of Mn(III) to Mn(IV) takes place as a consequence of the oxidising air atmosphere present, thus lowering Mn(III) and increasing Mn(IV). Further, both Mn(III) and Mn(IV) experience a proportionate

increase due to the increase in the total manganese content. Additionally, although limited, some thermal reduction of the material is possible at the higher temperatures considered, thereby causing slight increases to Mn(III) at the expense of Mn(IV). These processes superimpose to give the relatively steady Mn(IV) and slightly increasing Mn(III) content with respect to heat treatment temperature.

The proportions of water removed above and below 110°C '(%$H_2O$(>110°C)) and (%$H_2O$(<110°C)) respectively, further support these findings. The %$H_2O$(<110°C), which is water adsorbed on the surface of the material, generally decreases as heat treatment temperature increases, barring slightly higher values for the 300°C and 400°C materials relative to those around them. Clearly, the amount of water adsorbed to the surface of the material is largely determined by the available surface area and therefore it is no surprise that this result reflects the relative BET surface area for these samples (Table 1). The steady decrease in %$H_2O$(>110°C) (i.e., structural water associated with Mn(III) and vacancy defects) with heat treatment temperature provides a second, independent measure of the extent of structural water removal from the HEMD samples. By 350°C it appears that all structural defects that will be removed in the heat treatment have been, evidenced by the approximately constant %$H_2O$(>110°C) value for the 350°C and 400°C materials.

The trends in material properties discussed above are specific to a single EMD heat treated under the temperature/time determined from kinetic analysis. However, our investigation of the influence of the starting EMD properties on the resultant HEMD properties has shown these relationships to hold for a broad range of EMD materials [21].

### 4.3. Electrochemical performance

Due to the large number of cells tested (i.e., five HEMD materials each discharged at four currents), only the discharge characteristics of each HEMD at 2 mA/g are shown in Figure 11. The typically flat discharge curve of Li/$MnO_2$ at 2.8-3.0 V is evident from this plot. The primary discharge capacity (in mAh/g of $MnO_2$) for the cells tested was calculated by using a 2.0 V cut-off point. This result is shown in Table 4. As expected, the capacity of a given material decreases with higher discharge currents. On average the capacity for unheated EMD was 104 mAh/g (or 34% utilisation), which was less than half that of HEMD, with an average of 238 mAh/g (77% utilisation) at the 2 mA/g discharge rate. This clearly demonstrates the importance of the heat treatment process, as has been previously reported in the literature [22-24]. This vast difference in performance also suggests that EMD based cells are failing in a different way to HEMD cells. The high water content of the EMD likely leads to destructive side reactions with the electrolyte and anode causing cell failure. Conversely, HEMD is limited by the intrinsic material properties.

Considering the HEMD materials in greater detail, we note that manganese dioxide heat treated at 250°C and above maintained relatively good capacity at the higher discharge rates. Also of note are the excellent performance characteristics of the 300°C and 350°C materials particularly at the lower discharge rates. It was also observed that of the various HEMD samples, the material treated at 200°C exhibited relatively poor discharge capacities, this being especially noticeable at the higher discharge rates.

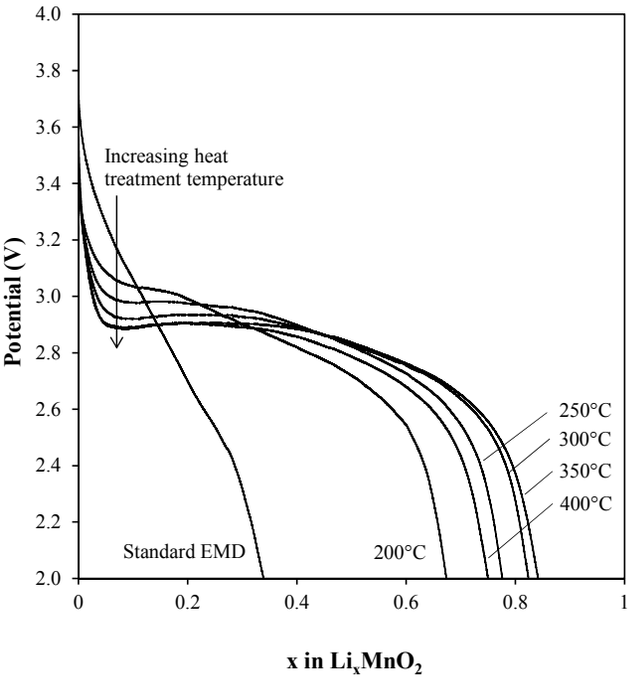


**Figure 11.** Discharge curves for heat treated EMD samples discharged at 2 mA/g.

| Temperature (°C) | Capacity (mAh/g) | | | |
|---|---|---|---|---|
| | 2 mA/g | 5 mA/g | 10 mA/g | 20 mA/g |
| 25 | 104.1 | 62.9 | 59.8 | - |
| 200 | 207.5 | 185.0 | 169.4 | 103.8 |
| 250 | 242.9 | 208.4 | 215.1 | 183.8 |
| 300 | 252.9 | 229.7 | 195.4 | 178.4 |
| 350 | 252.0 | 221.5 | 218.9 | 170.5 |
| 400 | 233.4 | 226.0 | 223.7 | 185.4 |

**Table 4.** Discharge capacity for heat treated EMD samples at various discharge currents (2.0 V cut-off).

Normalising the capacity of the cell in terms of the proportion of electrochemically active material (i.e., Mn(IV) percentage) reveals the extent to which the available material is being used. This will have a significant effect on the relative capacity of these HEMD materials since the proportion of Mn(IV) to Mn(III) has been seen to vary depending on the heat treatment conditions. The normalised capacities are listed in Table 5, and demonstrate that heat treatment at 300°C and 350°C has resulted in the highest proportion of electrochemically active Mn(IV) being utilised at the at 2 mA/g rate (94%).

Another useful way in which to present the data from these tests is through the use of a Ragone diagram, comparing the relative specific energy and power output of the materials. Due to the number of cells tested, only the points corresponding to the energy delivered by the cell by the cut-off voltage, and the corresponding power value, are shown in Figure 12. This diagram clearly shows a greater differentiation in energy delivered at the low discharge

rates, with the 300°C and 350°C materials exhibiting superior performance. Further, at high rates heat treatment at 250°C and above has resulted in materials exhibiting virtually equivalent performance. Comparison with literature Ragone diagrams [4] reveals that the performance of our materials is superior in terms of specific energy, and comparable in terms of specific power.

| Temperature (°C) | Utilization of Active Material | | | |
|---|---|---|---|---|
| | 2 mA/g | 5 mA/g | 10 mA/g | 20 mA/g |
| 25 | 0.39 | 0.23 | 0.22 | - |
| 200 | 0.77 | 0.69 | 0.63 | 0.39 |
| 250 | 0.87 | 0.75 | 0.77 | 0.66 |
| 300 | 0.94 | 0.85 | 0.73 | 0.66 |
| 350 | 0.94 | 0.83 | 0.82 | 0.64 |
| 400 | 0.89 | 0.86 | 0.85 | 0.71 |

**Table 5.** Utilization of active material (Mn(IV) percentage) for heat treated EMD samples at various discharge currents (2.0 V cut-off).

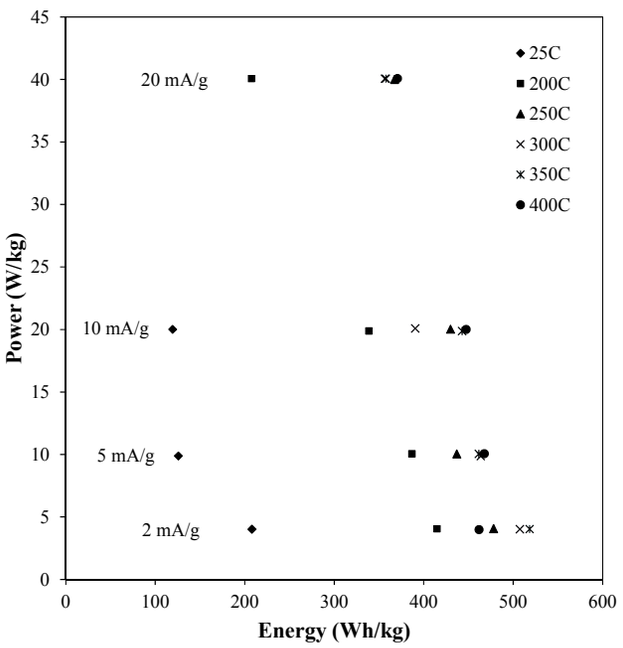


**Figure 12.** Ragone diagram showing points corresponding to energy delivered by the cell by the cut-off voltage and the corresponding power value for the heat treated EMD samples with respect to discharge rates.

As the electrochemical behaviour of manganese dioxide is largely dependent on the structure, composition and morphology of the material, the changes in these parameters with heat treatment temperature are invoked in explaining their relative electrochemical performance. Since the performance is not directly proportional to the heating temperature, it is immediately evident that there are a number of factors influencing material performance. From the current understanding of the Li/$MnO_2$ system, these factors are outlined as follows:

i. It is well known that the removal of both surface and structural water from the manganese dioxide structure is paramount, and that higher heating temperatures perform this function most completely and effectively [22].
ii. A greater amount of the more electrochemically active Mn(IV) species (compared to Mn(III)) is advantageous, and therefore materials in which oxidation of the Mn(III) to Mn(IV) has occurred will exhibit better performance.
iii. Samples retaining the γ-$MnO_2$ structure, with larger [1×2] tunnels in ramsdellite regions of the structure, are thought to provide both a greater degree of mobility and a larger number of insertion sites for ions introduced into the structure during discharge [25]. These relationships certainly hold for the aqueous system, although as yet there is currently no clear indication in the literature relating these structural features to the ease of lithium diffusion through materials used in the non-aqueous Li/$MnO_2$ system.
iv. The effect of sample porosity on the discharge characteristics of Li/$MnO_2$ cells remains relatively unknown. However, it has been previously determined that during heat treatment micro-pores within the EMD are sintered shut as a result of manganese ion movement, while the structural contraction connected with the phase transition from γ→β-$MnO_2$ and the increase in material density, induces cracking [18]. This results in an increase in the number of larger pores. These factors will be especially influential on the rate capabilities and total capacity of the cell [26].

In explaining the relative performance of the HEMD tested, each material will be considered separately and the above factors used to explain the resulting electrochemical performance. Some comparison will also be made highlighting differences between materials heat treated at consecutive temperatures and the effect these differences have had on the electrochemical performance. In the proceeding discussion, those materials exhibiting poorest performance will be discussed first, followed by the HEMD samples with better electrochemical characteristics.

From the physical characterisation of the 200°C material, it is clear that it has retained much of its original BET surface area, experienced some removal of cation vacancies, lost only a small amount of structural water, and maintained to a large extent the γ-$MnO_2$ parent structure. Of these features, the presence of structural water associated with cation vacancies and Mn(III) will be a limiting factor on the electrochemical performance. The water present evidently makes for poor performance at all discharge rates (on average 15% lower capacity than the 250°C material), highlighting the importance of its removal prior to use in Li/$MnO_2$ system. Perhaps an additional feature that limits the performance of this material is the relative ease of lithium ion movement in γ/β-$MnO_2$. While fundamental work has been performed analysing the mechanism and activation energy for proton diffusion in $MnO_2$ structures [25], these relationships are currently unknown for lithium diffusion in EMD/HEMD. The data presented here may indicate slower lithium ion diffusion through less pyrolusitic structures.

The properties of the 400°C material are very similar to the sample heat treated at 350°C; i.e., both samples have had basically all cation vacancies removed, with minor, but similar, amounts of structural water remaining, and both have experienced a high structural conversion to pyrolusite. However, an interesting difference is apparent in Figure 10, when

comparing the structural and morphological properties. Here, the sample heated at 400°C has maintained a larger unit cell and higher surface area compared to the 350°C material, most likely as a consequence of the shorter heating time applied to this material. This difference is likely responsible for its slightly lower performance at 2 mA/g (233 mA/g compared to 252-3 mA/g for the 300°C and 350°C materials). It is also possible that the conversion of γ-$MnO_2$ to a more pyrolusite-like structure as a consequence of the high heating temperature has been limiting on the performance. In conjunction with the low performance for the 200°C material, this may suggest that the optimum γ/β-$MnO_2$ structure for lithium insertion is not highly ramsdellitic or pyrolusitic structures, but rather some intermediate structure. From this, we propose an optimum value of $P_r$ for HEMD at low discharge rates, lying somewhere between 0.5 and 0.84, which leads to superior performance. At high rate discharge however, the 400°C material capacity is similar to the other materials, suggesting the differences in material properties have become more or less immaterial in determining the electrochemical performance.

The capacity of the material heat treated at 250°C (243 mAh/g) is higher the 400°C material (233 mAh/g) and slightly below the 300°C and 350°C materials (252-3 mAh/g) at the 2 mA/g discharge rate, but is essentially equal to them at high rates (~180 mAh/g at 20 mA/g). This is despite the fact that this material still contains reasonable amounts of structural water associated with both cation vacancies and Mn(III). The decreased capacity at the low rate can likely be attributed to the moderate retention of the γ-$MnO_2$ structure ($P_r$=0.52) which may limit the diffusion of lithium through the structure, although evidently to a lesser degree than in the 200°C material or the highly pyrolusitic 400°C structure. Additional differences between the 250°C material and those around it can be clearly seen in Figure 10. Noticeably, although the unit cell volume has not varied significantly between the 200°C and 250°C materials, the surface area has decreased by around 10%. This is largely due to a lower micropore volume in the 250°C material (Table 1). This feature would likely aid the discharge of this material since the small micro-pores can only accommodate a limited number of lithium ions. Hence, when the cell is discharged, the few ions in these pores are soon inserted into the structure. The subsequent deficiency of lithium ions in this locality limits the discharge capabilities of the cell, especially at high discharge rates.

The materials heat treated at 300°C and 350°C demonstrated the highest capacity over the range of discharge rates tested. Relating this back to the properties, the 300°C material had a moderate amount of defects remaining in the structure, with a pyrolusite to ramsdellite ratio of 0.73. The particular structural arrangement is likely of particular significance in light of the poorer performance of materials with low or high $P_r$ values (e.g., 200°C and 400°C materials, respectively). Also of interest are the relationships between the structural and morphological features of the 300°C sample (Figure 10). This data suggests that this material has undergone significant amounts of structural rearrangement (shown by a smaller unit cell), but maintained a relatively high surface area (31 $m^2/g$). The combination of the structural arrangement, composition and surface area has resulted in this material delivering one of the highest capacities at low discharge rates, with comparable performance at high rates.

Finally, as we have already noted the material properties of the 350°C material are similar to that of the 400°C sample in terms of composition, although key differences are noted in the structure and morphology, as highlighted in Figure 10. These differences are significant in light of the superior electrochemical characteristics of the 350°C material. Figure 10 shows that heat treatment at 350°C has resulted in the greatest contraction of the unit cell and also a lowering of the BET surface area relative to the other HEMD materials. The smaller unit cell is the main structural difference between the 350°C and 400°C materials, which otherwise have very similar $P_r$ values (0.83 and 0.84, respectively). This suggests that the proportion of each phase is not the only structural feature influencing the movement of lithium ions through the material, and that the unit cell volume is also significant. The high performance of the 350°C material is an indication that lower unit cell volumes are favoured for lithium diffusion in HEMD. The morphology differences between these materials are also likely to play a significant role in determining their relative electrochemical performance. As previously noted, the lower BET surface area for the 250°C sample due to a lower volume of micropores, was found to enhance its capacity over the 200°C material. Similarly, the change in morphology brought about by the removal of these micropores in the 350°C material has clearly improved the material capacity across discharge rates.

## 5. Conclusion

In conclusion, this work has shown that kinetic analysis can be employed in optimising the thermal processing of positive electroactive materials. As an example, kinetic analysis using a first-order kinetic analysis method and an incremental integral approach was performed for the water loss process from electrolytic manganese dioxide, the precursor material for use in non-aqueous Li/$MnO_2$ cells. Both methods determined the pre-exponential factor and the activation energy for this process as a function of the extent of conversion, hence allowing for variation in the values over the process studied, while the incremental integral method also varied with heating rate.

Comparison and investigation of the two methods revealed the incremental integral method as the preferred means for obtaining the kinetic parameters describing this process. This result stems back to the use of a single TG experiment and the exclusive use of a slower scan rate using the incremental integral method (multiple scan rates, and thus experiments, are required in the first order kinetic analysis method). A single experiment avoids inherent variability between multiple experiments and limits errors induced in the somewhat arbitrary application of the background correction. Using slower scan rates reduces the possible undesired effects arising from thermal gradients across the sample as a result of the thermal conductivity of the material.

Using the kinetic parameters determined for this process, and assuming first order kinetics, a family of thermal treatment regimes based on heating temperature and duration were calculated to, in theory, completely remove water from the manganese dioxide structure.

Characterization of the resulting HEMD materials revealed considerable differences in their properties. It was found that materials undergo a mainly kinetically limited thermal

conversion from γ-$MnO_2$ towards β-$MnO_2$. The material surface area generally decreases with heating temperature, although noticeably, the pore collapse process is thermally limited at lower temperatures, while at the higher temperatures the reaction kinetics dictate the extent to which this process proceeds. Despite the theoretical expectation of complete water removal from the EMD, experimental results demonstrate that thermal and kinetic limitations present under these heating conditions prevent the completion of the water loss process. In general, however, as heating temperature increases there is a decrease in cation vacancy fraction and amount of structural water, while Mn(III) and Mn(IV) increase and remain relatively steady, respectively.

Electrochemical performance of the HEMD materials generated in this work revealed they are superior in terms of specific energy, and comparable in terms of specific power, to recent reports in the literature for the primary Li/$MnO_2$ system. Greatest differentiation of materials was noted at the low discharge rates, where materials prepared at 300°C and 350°C demonstrated best performance.

Finally, it is important to note that the method of kinetic analysis outlined here is not limited to only mass loss processes. It can in fact be employed to monitor the progress of any thermally based reaction which undergoes changes measurable by TG, DTA, DSC, etc. Therefore, the method of kinetic analysis outlined here could be applied in optimising the preparation and electrochemical performance of numerous other positive electroactive materials with similar improvements to performance anticipated.

## Author details

Wesley M. Dose and Scott W. Donne
*Discipline of Chemistry, University of Newcastle, Callaghan, Australia*

## Acknowledgement

The authors would like to acknowledge the University of Newcastle EM-X-ray Unit and Ms. Jenny Zobec for assistance in obtaining the XRD data. WMD acknowledges the University of Newcastle for the provision of an APA PhD scholarship.

## 6. References

[1] Lewis N.S (2005) Scientific Challenges in Sustainable Energy Technology, Keynote address at 208th meeting elecrochem. soc., Los Angeles.
[2] Ristinen R.A, Kraushaar J.P (2005) Energy and the Environment. 2nd Ed. USA: Wiley.
[3] Ragone D (1968) Review of Battery Systems for Electrically Powered Vehicles. SAE Technical Paper 680453. doi:10.4271/680453.
[4] Simon P, Gogotsi Y (2008) Materials for Electrochemical Capacitors. Nat. mater. 7: 845-854.
[5] Linden D, Reddy T.B, editors (2001) Handbook of Batteries. 3rd ed. USA: McGraw-Hill.
[6] Whittingham M.S (2004) Lithium Batteries and Cathode Materials. Chem. rev. 104: 4271-4301.

[7] Kim D.H, Kim J (2006) Synthesis of $LiFePO_4$ Nanoparticles in Polyol Medium and Their Electrochemical Properties. Electrochem. solid-state lett. 9: A439-A442.
[8] Wickham D.G, Croft W.J (1958) Crystallographic and Magnetic Properties of Several Spinels Containing Trivalent JA-1044 Manganese. J. phys. chem. solids. 7: 351-360.
[9] Chabre Y, Pannetier J (1995) Structural and Electrochemical Properties of the Proton/γ-$MnO_2$ System. Prog solid state chem. 23: 1-130.
[10] Brunauer S, Emmett P.H, Teller E (1938) Adsorption of Gases in Multimolecular Layers. J am chem soc. 60: 309-319.
[11] Vogel A.I (1989) Quantitative Chemical Analysis. New York: John Wiley & Sons.
[12] Williams R.P (1995) Characterisation and Production of High Performance Electrolytic Manganese Dioxide for use in Primary Alkaline Cells. PhD Thesis, University of Newcastle, Australia.
[13] Fraioli A.V (1985) Investigation of Manganese Dioxide as an Improved Solid Desiccant. Proc. electrochem. soc. 85-4: 342-368.
[14] Budrugeac P, Segal E (2001) Some Methodological Problems Concerning Nonisothermal Kinetic Analysis of Heterogeneous Solid-Gas Reactions. Int. j. chem. kinet. 33: 564-73.
[15] Simon P, Thomas P.S, Okiliar J, Ray A.S (2003) An Incremental Integral Isoconversional Method. J. therm. anal. calorim. 72: 867-874.
[16] Haynes W.M, editor (2009) CRC Handbook of Physics and Chemistry. 91st ed. USA: CRC Press.
[17] Maciejewski M (2000) Computational Aspects of Kinetic Analysis. Part B: the ICTAC Kinetics Project B - the Decomposition Kinetics of Calcium Carbonate Revisited, or Some Tips on Survival in the Kinetic Minefield. Thermochim. acta. 355: 145-154.
[18] Arnott J.B, Williams R.P, Pandolfo A.G, Donne S.W (2007) Microporosity of Heat-Treated Manganese Dioxide. J. power sources. 165: 581-590.
[19] Malloy A.P, Browning G.J, Donne S.W (2005) Surface Characterization of Heat-Treated Electrolytic Manganese Dioxide. J. colloid. interface. sci. 285: 653-664.
[20] Bystrom A.M (1949) Crystal Structure of Ramsdellite, an Orthorhombic Modification of Manganese Dioxide. Acta chem. scand. 3: 163-173.
[21] Dose W.M, Donne S.W (2011) Heat Treated Electrolytic Manganese Dioxide for Li/$MnO_2$ Batteries: Effect of Precursor Properties. J. electrochem. soc. 158: A1036-A1041.
[22] Ikeda H, Saito T, Tamura H (1975) Manganese Dioxide as Cathodes for Lithium Batteries. Manganese dioxide symp. [proc.]. 1: 384-401.
[23] Ilchev N, Manev V, Hampartzumian K (1989) The Lithium-Manganese Dioxide Cell II. Behaviour of Manganese Dioxide in Nonaqueous Electrolyte. J. power sources. 25: 177-185.
[24] Ohzuku T, Kitagawa M, Hirai T (1989) Electrochemistry of Manganese Dioxide in Lithium Nonaqueous Cell. J. electrochem. soc. 136: 3169-3174.
[25] Balachandran D, Morgan D, Ceder G (2002) First Principles Study of H-Insertion into $MnO_2$. J. solid state chem. 166: 91-103.
[26] Lee T.J, Cheng T.T, Juang H.K, Chen S.Y (1993) Relationship of Cathode Pore-Size Distribution and Rated Capacity in Lithium/Manganese Dioxide Cells. J. power sources. 43-44: 709-712.